

www.acsami.org Research Article

Direct Observations of Uniform Bulk Heterojunctions and the Energy Level Alignments in Nonfullerene Organic Photovoltaic Active Layers

Rabindra Dulal, William R. Scougale, Wei Chen, Ganesh Balasubramanian, and TeYu Chien*



Cite This: ACS Appl. Mater. Interfaces 2021, 13, 56430–56437



ACCESS More Article Recommendations Supporting Information Distance (nm) $E_F = 0.8 \text{ eV}$ $E_F = 0.71 \text{ eV}$ $E_G = 2.54 \text{ eV}$ $E_G = 1.8 \text{ eV}$

ABSTRACT: State-of-the-art organic photovoltaic (OPV) cells rely on the engineering of the energy levels of the organic molecules as well as the bulk-heterojunction nanomorphology to achieve high performance. However, both are difficult to measure inside the active layer where the electron donor and acceptor molecules are mingled. While the energy level alignments of the lowest unoccupied molecular orbital (LUMO) and highest occupied molecular orbital (HOMO) between the electron donors and acceptors may be altered in the mixed active layer compared to their pure forms, the nanomorphology of the donor and acceptor molecular domains is mostly studied in indirect means. Here, we present the direct observations of the nanomorphology of the molecular domains as well as the energy level alignments in the active layer of a nonfullerene-based OPV (donor: PBDB-T-2F and acceptor: IT-4Cl) using cross-sectional scanning tunneling microscopy and spectroscopy (XSTM/S). It is revealed that (1) the bulk-heterojunction (BHJ) structures are homogeneous and uniform throughout the \sim 1.2 μ m thick active layer; (2) the energy alignments between the donor-rich and acceptor-rich domains are directly observed; (3) there exist the intermixing domains at the boundaries of the donor-rich and acceptor-rich domains with thickness in the nm scale; (4) the exciton binding energies in PBDB-T-2F and IT-4Cl are estimated to be 0.74 and 0.32 eV, respectively; and (5) there is an \sim 0.7 V loss in the open circuit voltage. The results provide a nanoscale understanding of the OPV active layers to guide further improvement of the OPV performance.

KEYWORDS: organic photovoltaic, cross-sectional scanning tunneling microscopy and spectroscopy, quasi-random structures, nanomorphology, bulk heterojunction

■ INTRODUCTION

With the advantages of environmental friendliness, flexibility, and low cost of production, organic photovoltaic (OPV) cells are considered as one of the most promising next-generation photovoltaic technologies. Previous reports mostly focused on designing new materials, ^{1–5} device structures, ^{6,7} and processing techniques ^{8–10} to improve the power conversion efficiency (PCE). In the material designs, significant advances have been made to various donor polymers. ^{11–13} On the other hand, the development of the acceptors lags behind, with the major efforts devoted to the chemical modification of the fullerene family. ^{1,14–17} So far, fullerene-based OPVs exhibit PCE up to 10–11%. ^{18,19} It is recognized that the fullerene derivatives have some drawbacks as the electron acceptors for the OPV operation: weak absorption coefficient in the visible light region, difficult synthesis and purification, ²⁰ air sensitivity, ^{21,22}

and their inherently low lowest unoccupied molecular orbital (LUMO) energy levels. ^{23,24} This leads to the development of the nonfullerene small molecules for being used as the acceptors. Up to date, the reported nonfullerene-based OPVs have achieved PCE over 18%. ^{25–27}

The engineering of the energy level alignment between the electron donors and acceptors is the key guidance in designing new molecules for OPV applications. The ideal band

Received: September 23, 2021 Accepted: November 3, 2021 Published: November 17, 2021





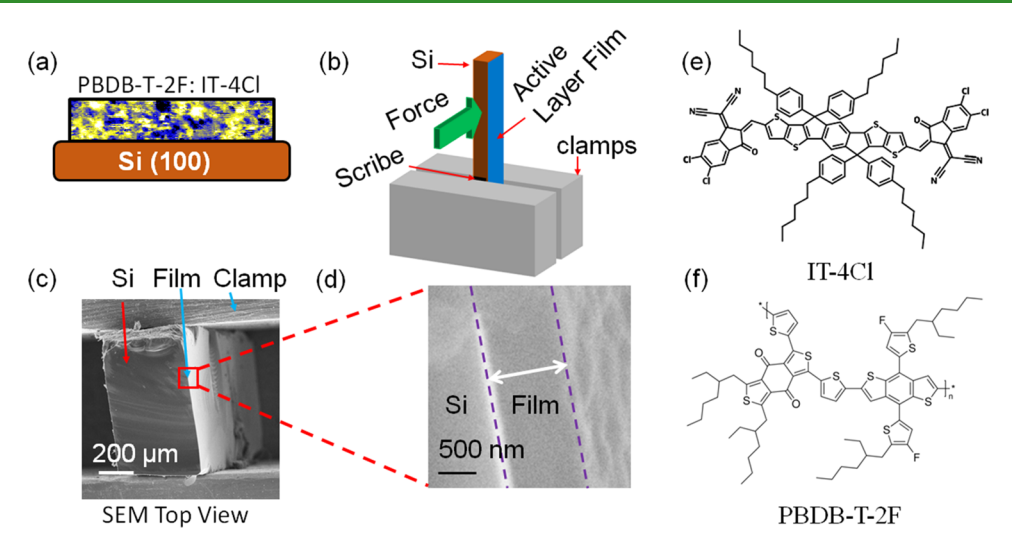


Figure 1. (a) Schematics of the prepared active layer on top of a Si(100) substrate. (b) Experimental setup of the sample holder and the sample for the XSTM/S measurements. (c) SEM image of the cross-sectional view of the fractured sample. (d) SEM image of the zoomed-in view near the red rectangular region in panel (c). Panels (e) and (f) show the molecular structure of IT-4Cl and PBDB-T-2F, respectively.

relationship between the donors and acceptors is the type II staggered gap in the semiconductor interfaces. During the exciton dissociation process in a bulk-heterojunction (BHJ) nanomorphology, electrons hop from the LUMO of the donor to the LUMO of the acceptor and holes hop from the highest occupied molecular orbital (HOMO) of the acceptor to the HOMO of donor. It was pointed out that the open circuit voltage is related to the energy alignment as

$$e \cdot V_{OC} = LUMO(A) - HOMO(D) - \Delta$$
 (1)

where e is the elementary charge and Δ is a loss term, which has been suggested to be related to the exciton binding energy²⁸ or radiative and nonradiative temperature-dependent losses. 29-31 The HOMO(D)/LUMO(A) offset is denoted in various ways in the literature, such as charge-transfer gap, intermolecular gap, or donor/acceptor gap. It is often estimated by optical spectroscopy^{31,32} or electrical characterization, e.g., cyclic voltammetry,³² reverse saturation current analysis,^{28,33} or temperature-dependent measurements of the open circuit voltage.^{31,34} All of these studies assumed that the interfaces of the donor and acceptor molecules are sharp. However, the nm scale domain transition from donor to acceptor in the P3HT/PCBM mixture was observed by crosssectional scanning tunneling microscopy and spectroscopy (XSTM/S).³⁵ With these information, the charge separation dynamics and the geminate recombination across the donoracceptor domain interfaces can be modeled in a more precise way. Also, with the direct observation of the HOMO(D)/ LUMO(A) offset, the loss term, Δ , can be more accurately determined. Ways to reduce the loss term will then be possible. With the newly developed nonfullerene acceptors, it is important to extend our knowledge of the similar nanoscale energy level alignment in the nonfullerene-based OPVs. Here, we utilize the XSTM/S to directly reveal the spatial evolution of the HOMO and LUMO of the nonfullerene-based OPVs. We choose PBDB-T-2F and IT-4Cl because it has been reported with a high PCE of 12.67 and 13.45% in two independent studies.36,37

BHJ architecture in the OPV active layers is believed to be responsible for the high efficiency due to its quasi-random nanomorphology, which facilitates charge separation for the

short exciton mean free path in the organic molecules.³⁸ In the BHI design, electron donor and acceptor molecules form donor-rich and acceptor-rich domains^{39,40} in the length scale similar to the exciton mean free path. The BHJ nanomorphology can be studied and reproduced in computational studies. 40-44 On the other hand, it is usually indirectly observed experimentally by X-ray diffraction (XRD), atomic force microscopy (AFM),⁴⁵ scanning electron microscopy (SEM),46 and transmission electron microscopy (TEM).4 XSTM/S is an ideal tool to study BHJ since it is capable of providing high spatial resolution (atomic or nm scale) with molecule sensitivity (probing the HOMO, LUMO energy levels). 48 Various studies explored the thickness effects on the PCE. 49-57 However, the depth evolution of the BHJ nanomorphology is seldom discussed and is assumed homogeneous in most cases. The annealing process used in synthesizing the active layer involves the evaporation of the solvent molecules and the redistribution of the donor and acceptor molecules. Since the solvent molecules need to pass through the active layer during this process, it is expected that the dynamics of the solvent molecule evaporation is inhomogeneous throughout the thickness; hence, the nanomorphology may be potentially inhomogeneous. The inhomogeneous BHJ nanomorphology has two competing effects on the PCE. First, the exciton charge separation prefers the molecular domain sizes to be smaller than the exciton diffusion length (~5 nm in the P3HT/PCBM case). In the inhomogeneous BHJ nanomorphology case, larger domain sizes at certain depths have a negative impact on the charge separation efficiency. Second, the charge collection process is limited by geminate recombination, in which electrons and holes in the electron acceptor and donor domains, respectively, recombined across the donor-acceptor interfaces. The larger domain sizes in the inhomogeneous BHJ nanomorphology at different depths may reduce this geminate recombination by reducing the interface area. Clear evidence of the homogeneity of the BHJ nanomorphology is crucial information to understand the OPV active layer. Here, the depth evolution of the BHJ nanomorphology is also revealed and analyzed by XSTM/S measurements. It is found that the BHJ nanomorphologies are homogeneous and uniform throughout an

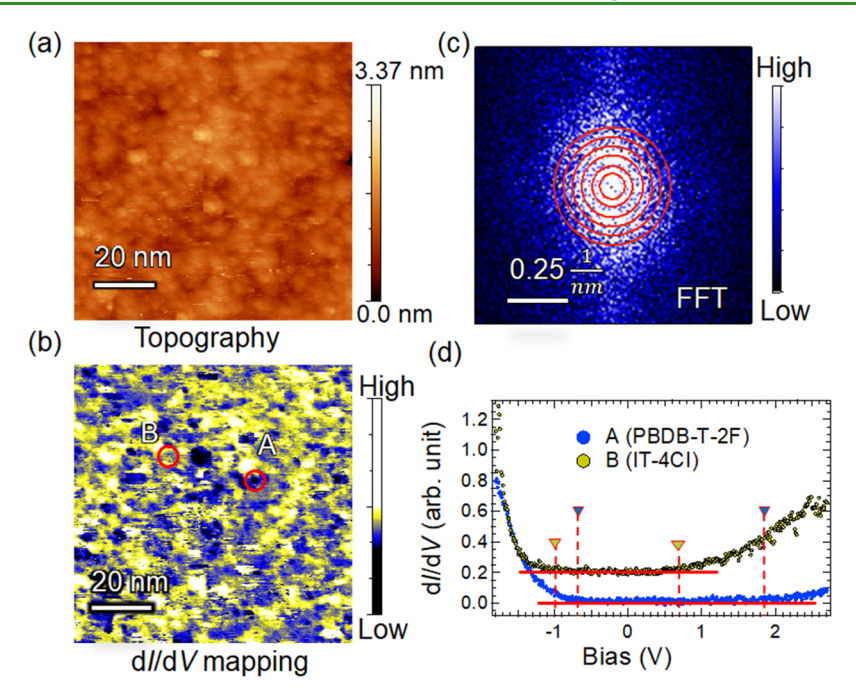


Figure 2. (a) STM topography and (b) dI/dV mapping of the PBDB-T-2F:IT-4Cl active layer. Scanning condition: $V_{\text{bias}} = 2 \text{ V}$, $I_{\text{tunneling}} = 300 \text{ pA}$. (c) Fast Fourier transform image of panel (b). (d) dI/dV point spectra measured at high- and low-contrast regions indicated by the red circles in panel (b).

 \sim 1.2 μ m thick nonfullerene active layer. This result provides strong confidence that the nanomorphology of the molecular domains in the thinner active layer should also be homogeneous. With this observation technique, it is then possible to design an inhomogeneous BHJ structure and its influence on the PCE.

METHODS

PBDB-T-2F (used as received from Ossila) and IT-4Cl (used as received from Ossila, purity >99%) were made into separate solutions in o-xylene (used as received from Sigma-Aldrich) with 7 mg/mL concentration. Solutions with the PBDB-T-2F:IT-4Cl weight ratio 1:1 were then made by mixing the precursor solutions, followed by spin coating onto a Si(100) substrate with 1050 rpm for 1 min. The PBDB-T-2F:IT-4Cl/Si(100) films were annealed at 100 °C for 10 min in an inert (Ar) environment. Figure 1a illustrates the prepared sample for characterizations. The STM measurements were performed using the XSTM/S method^{48,58-60} to prevent air exposure of the interior of the thin films. Figure 1b shows the XSTM/S sample holder and sample setup. A scribe is made on the side of a Si(100) substrate (8 mm \times 1 mm \times 0.5 mm) prior to the spin coating. The spin coating was performed by placing four cut pieces on the sticky tape on top of the spin coater. Each piece was placed back to the exact order as they were cut to create a gapless substrate for spin coating. The mounted samples were fractured in situ under an ultrahigh vacuum (UHV) environment with a base pressure of 10^{-10} mbar prior to the STM measurements. All of the data were collected at room temperature using the Omicron low-temperature STM system with a base pressure of 10^{-10} mbar. dI/dV signals were recorded with a 1997 Hz modulation frequency, a 1 ms time constant, and a 100 meV voltage modulation in the lock-in settings. STM topography and dI/ dV images were collected simultaneously with 450 \times 450 pixels. The STM topography images and dI/dV mappings were analyzed using WSXM software. 61 After the STM measurements, scanning electron microscopy (SEM) measurements were carried out with the JEOL 5800 LV SEM. Figure 1c shows the SEM image of the top view of the fractured surfaces (e.g., the cross-sectional view of the thin film). A zoomed-in view of Figure 1c is shown in Figure 1d, where the active layer thin film is clearly seen and the thickness is determined to be

 \sim 1.1 μ m. Note that the thickness of the active layer varies at different locations, ranging from 1 to 1.2 μ m (see Figure S1).

RESULTS AND DISCUSSION

Figure 2a,b shows the 100 nm × 100 nm scale XSTM/S topography and the dI/dV mapping of the prepared PBDB-T-2F:IT-4Cl layer, respectively. The topography root-meansquare (RMS) roughness of the fractured active layer is determined to be ~0.2 nm. The distributions of the electron donor-rich and acceptor-rich domains are observed in the dI/ dV mapping (Figure 2b) and are confirmed as the BHJ structure. Figure 2c shows the fast Fourier transform (FFT) image of the dI/dV mapping (Figure 2b). It is further confirmed that the molecular domains are isotropic through the analysis of the FFT image by fitting it with a twodimensional (2D) rotated ellipse Gaussian function as

$$F(k_{x_{i}}k_{y}) = A$$

$$e^{-\left(\frac{\left((k_{x}-k_{x_{0}})\sin(\theta)+(k_{y}-k_{y_{0}})\cos(\theta)\right)^{2}}{a^{2}} + \frac{\left((k_{x}-k_{x_{0}})\cos(\theta)-(k_{y}-k_{y_{0}})\sin(\theta)\right)^{2}}{b^{2}}\right)}$$
(2)

where A is the intensity; a and b are the lengths of the major and minor axes, respectively; k_{x_0} and k_{y_0} describe the coordinates of the center; and θ is the angle between the major axis and x-axis. 48 The fitting result is displayed as the red contour plots in Figure 2c. The isotropy is quantified using the

eccentricity
$$\left(\in = \sqrt{1 - \left(\frac{b}{a}\right)^2} \right)$$
, as 0.1 \pm 0.1. The close to

zero value of ϵ indicates an isotropic texture. The eccentricity is also analyzed for 10 other independent dI/dV mappings measured at various locations, resulting in an eccentricity of 0.17 ± 0.05 (see details in the Supporting Information, Table S1). The slight deviation from zero value is believed to be due to the artifacts caused by the horizontal scanning direction. Specifically, the horizontal scanning direction results in the

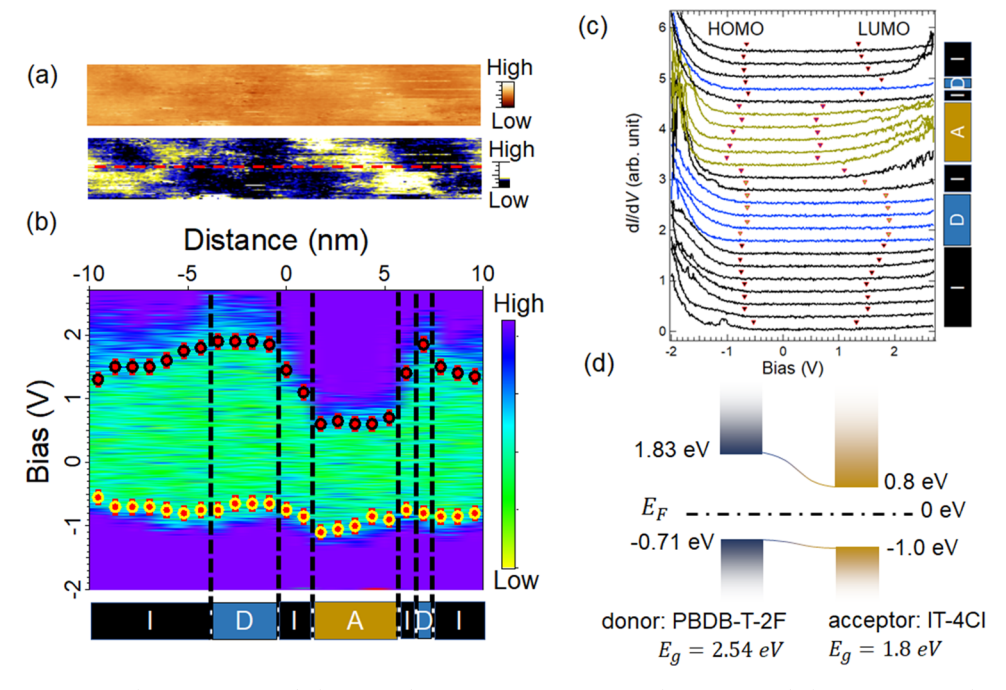


Figure 3. (a) STM topography (20 nm \times 2.5 nm) (top panel) and the dI/dV mapping (bottom panel) (20 nm \times 2.5 nm). Scanning condition: $V_{\text{bias}} = -2 \text{ V}$, $I_{\text{tunneling}} = 300 \text{ pA}$. (b) Grid spectra taken along the red dashed line across the region shown in panel (a). The yellow circles and the black circles represent the HOMO and LUMO energy levels, respectively, at each spectrum. (c) dI/dV spectra of the grid measurements. The inverted triangles representing the HOMO and LUMO energy levels of each spectrum. (d) Schematics of the band alignments between the donor and acceptor regions.

horizontal streakiness lines seen in Figure 2b and end up as slight elongation in the vertical direction in the FFT image shown in Figure 2c. In short, an isotropic BHJ is observed in the PBDB-T-2F:IT-4Cl active layer.

The assignment of the donor-rich and acceptor-rich domains is based on the dI/dV point spectra measured at the corresponding locations. Figure 2d shows the dI/dV point spectra taken at the marked locations in Figure 2b. The blue curve represents the spectrum taken at a blue region (lowcontrast region), while the yellow curve represents the spectrum taken at a yellow region (high-contrast region) in the dI/dV mapping (Figure 2b). The HOMO and the LUMO energy levels in each spectrum are analyzed at the onset bias of the dI/dV signals and indicated by the inverted triangles shown in Figure 2d. The blue region (lower dI/dV contrast region) exhibits an energy gap of 2.55 ± 0.05 eV and higher HOMO and LUMO energies compared to that of the yellow region (higher dI/dV contrast region), where the energy band gap is determined to be 1.70 ± 0.05 eV. The energy level alignment is the typical type II staggered gap in the semiconductor interfaces. Clearly, based on this observation, the low-contrast region (blue region) is assigned to the electron donor-rich (PBDB-T-2F) regions, while the high-contrast region (yellow region) is assigned to the acceptor-rich (IT-4Cl) regions.

Both the observed band gaps for IT-4Cl $(1.70 \pm 0.05 \text{ eV})$ and for PBDB-T-2F $(2.55 \pm 0.05 \text{ eV})$ are larger than the reported optical band gaps: 1.48 eV for IT-4Cl³⁶ and 1.80 eV for PBDB-T-2F.⁶² It is known that the optical band gap is typically smaller than the electronic band gap, with the difference accounted as the exciton binding energy^{63,64}

$$E_{\rm g} = E_{\rm abs} + E_{\rm b,exc} \tag{3}$$

where E_g is the electronic band gap; E_{abs} is the optical band gap measured by absorption spectrum; and $E_{b,exc}$ is the exciton

binding energy. It has been reported that many small acceptor molecules have small exciton binding energies, such as ITIC (0.25 eV), IDIC-4Cl (0.25 eV), 6TIC-4F (0.16 eV), and 4TIC (0.04 eV), 65 while the donor polymers have large exciton binding energies, such as an \sim 0.7 eV exciton binding energy in P3HT. 63,66 Following eq 3, with the dI/dV-extracted electronic band gaps and the reported optical band gap measured by absorption spectrum, one may extract the exciton binding energies in PBDB-T-2F and IT-4Cl, which will be discussed later. To further accurately determine the electronic band gaps in the two molecular domains, we performed a detailed dI/dV grid spectrum measurement across the molecular domains to obtain the statistical results of the energy gaps.

Figure 3a shows the topography (top) (20 nm \times 2.5 nm) and dI/dV mapping (bottom) (20 nm × 2.5 nm) of the PBDB-T-2F:IT-4Cl active layer. The contrast in the dI/dV mapping clearly shows the donor-rich and acceptor-rich domains. dI/dVpoint spectra are measured along a red dashed line shown in the dI/dV mapping of Figure 3a, with a spacing between each location of the measured spectrum as 0.9 nm. The resulting spectra and the energy levels of the HOMO and LUMO of each spectrum are analyzed and shown in Figure 3b,c. Donorrich (low contrast in dI/dV mapping in Figure 3a and labeled as "D" in Figure 3b,c) and acceptor-rich (high contrast in dI/ dV mapping in Figure 3a and labeled as "A" in Figure 3b,c) regions exhibit the expected energy gaps and band alignment, as shown in Figure 2d. In addition to that, there exists an intermediate region sandwiched between the donor-rich and acceptor-rich regions, indicated as "I" in Figure 3b,c. This intermediate region has a band gap in between the "D" and "A" regions, and the spectrum evolves spatially from "D" to "A" regions smoothly with a length scale of a few nm. This indicates that the intermediate regions may simply be the transition of the spatial evolution of the molecular

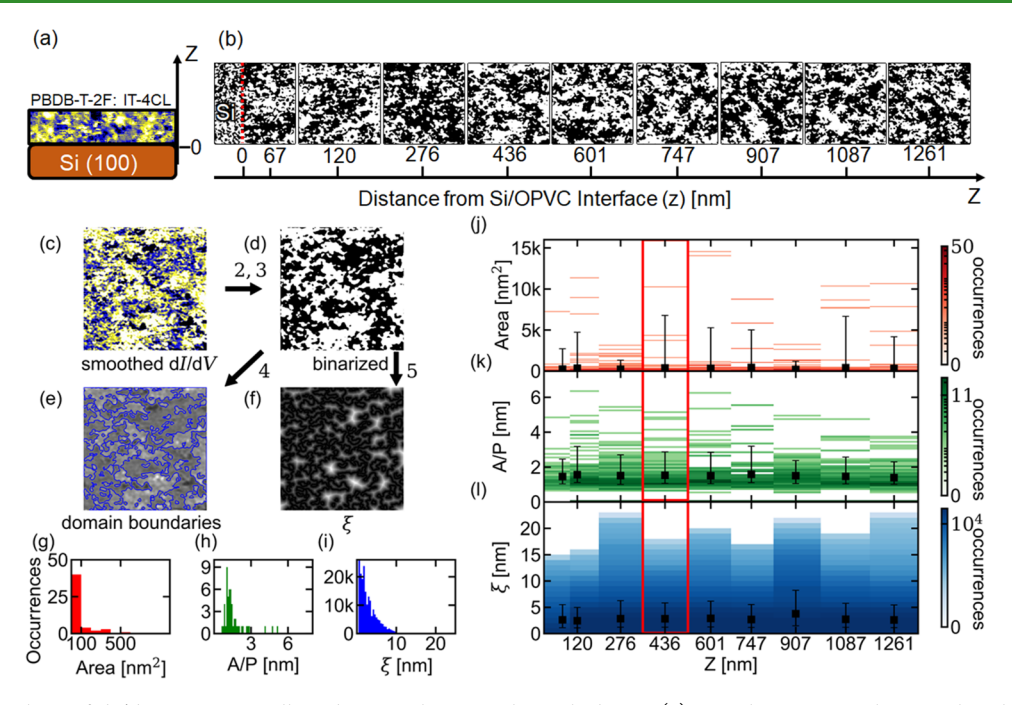


Figure 4. Image analysis of dI/dV mappings collected across the active layer thickness. (a) Sample geometry showing the silicon substrate, the active layer, and the definition of z. (b) Binarized dI/dV mappings as a function of z from the Si/active layer interface to the top of the active layer in the cross-sectional geometry. The image evolution through the processing procedure from (c) smoothed, (d) binarized dI/dV mapping, and the analyzed (e) domain boundary identification and (f) distance (ξ) to the nearest D/A interface. The histograms of the physical quantities—(g) domain area, (h) domain area/perimeter ratio, and (i) distance (ξ) to the nearest D/A interface are extracted from the processed images. The z-dependent evolutions of the histograms of these quantities are shown in panels (j-l). The color maps of occurrence are plotted on a log scale for clarity. The mean values and ranges are plotted in black dots and bars, respectively, for each data set.

compositions from acceptor-rich gradually to donor-rich regions. The interfacial electron band alignments between "D" and "A" regions at the nm scale in active layers of OPVs are not sharp and should have great impacts on understanding the influences on the OPV charge separation and recombination mechanisms.

With detailed analysis, the donor-rich region (PBDB-T-2Frich region) has the LUMO at 1.83 \pm 0.09 eV and the HOMO at -0.71 ± 0.06 eV, while the acceptor region (IT-4Cl rich region) has the LUMO at 0.8 ± 0.1 eV and the HOMO at -1.0 ± 0.1 eV. This gives the energy offset between the donor and acceptor domains of LUMO_D-LUMO_A = $1.0 \pm 0.1 \text{ eV}$, $HOMO_D - HOMO_A = 0.3 \pm 0.1 \text{ eV}$, and $LUMO_A - HOMO_D =$ 1.5 ± 0.1 eV. The band alignments between the donor and acceptor regions are also summarized in Figure 3d. In previous works, HOMO_D-HOMO_A between PBDB-T-2F and IT-4Cl were estimated to be 0.3³⁶ and 0.28 eV,³⁷ respectively, which are consistent with our results. However, the LUMO_D-LUMO_A between PBDB-T-2F and IT-4Cl were estimated as 0.62³⁶ and 0.42 eV,³⁷ respectively, which are smaller than our results. Since, in the previous works, the LUMO levels were estimated by the HOMO levels and the optical band gaps, it is possible that the discrepancy originates from the unaccounted exciton binding energy (will be discussed in the next paragraph). As mentioned in eq 1, the open circuit voltage, $V_{\rm OC}$, is related to the energy alignments between the donor and acceptor and a loss term, Δ. With the LUMO_A-HOMO_D = 1.5 \pm 0.1 eV from our data and $V_{\rm OC}$ = 0.790 V^{36} and $V_{\rm OC}$ = 0.78 V^{37} from previous works, the loss term, Δ , can be determined to be 0.71-0.72 eV. The source of the loss is potentially related to the exciton binding energies. Further studies are needed to identify the detailed contribution of the loss term.

The exciton binding energies can be estimated from our data when compared with the reported optical absorption spectra. The band gaps for the PBDB-T-2F-rich region, the IT-4Cl-rich region, and the intermediate region are determined as 2.54 ± 0.09, 1.8 ± 0.1 , and 2.3 ± 0.1 eV, respectively. Following eq 3, with the dI/dV-extracted electronic band gaps (2.54 \pm 0.09 eV for PBDB-T-2F and 1.8 \pm 0.1 eV for IT-4Cl) and the reported optical band gap measured by absorption spectrum (1.80 eV for PBDB-T-2F⁶² and 1.48 eV for IT-4Cl³⁶), one can extract the exciton binding energies in PBDB-T-2F and IT-4Cl as 0.74 and 0.32 eV, respectively. The difference between the two exciton binding energies (~0.4 eV) is accounted for the discrepancy between our results (exciton binding energies accounted) and the results from previous works (exciton binding energies unaccounted) discussed above regarding the LUMO_D-LUMO_A.

Depth Evolution of the Molecular Domain Nanomorphology. The depth evolution of the nanomorphology of the molecular domains in the active layer is observed by taking the dI/dV mappings as a function of the distance to the Si substrate/active layer interfaces in the cross-sectional geometry. Figure 4a shows a schematics illustrating the definition of the \hat{z} direction as the active layer thin film normal direction and z=0 is set at the interface with the Si substrate. Figure 4b shows the evolution of the nanomorphology of the molecular domains from the interface (z=0) to the surface of the active layer $(z=\sim 1200 \text{ nm})$ with a scale of 200 nm \times 200 nm. The positions of images in Figure 4b are labeled based on the distance measured from the center of that image to the Si/active layer interface, as identified in the first image shown in

Figure 4b, which is enlarged and shown in Figure S2. Typical OPV active layers are on the order of a few hundreds of nm. We chose to examine this thickness for the active layer as to maximize the solvent molecular evaporation influence on the nanomorphology during the annealing process. In Figure 4b, the STM dI/dV mappings are processed with the following procedures: (1) smoothed with a Gaussian function with 10 pixel width to remove the noise; then, (2) the images are binarized using the method described in the previous work;⁴⁰ after binarization, (3) domains with an area less than 10 nm² were filtered out by including them in the surrounding domains (the 10 nm² chosen for this filtering process is to remove the single-pixel spike noise-induced domains through the smoothing procedure; step (1)); then, (4) the domain boundaries, the domain areas, and the domain perimeters were determined using contour analysis; and (5) the distances of each pixel to the nearest D/A interfaces were analyzed. The raw and smoothed dI/dV mappings are shown in Figure S4. The binarized dI/dV mappings were processed and analyzed to extract the domain sizes, perimeter lengths, and the distances from each pixel to the nearest D/A interfaces using Python 3 and the image processing package Open CV2.67 The detailed analysis of the processed images is shown in Figures S5-S21. The statistics of the area, area-to-perimeter ratio (APR), and the distance to the nearest D/A interfaces of Figure 4c are illustrated in Figure 4g-i, respectively. From Figure 4g-i, the values of the area, the APR, and the distance to the D/A interfaces (ξ) are determined to be 320 \pm 80 nm², 1.5 \pm 0.1 nm, and 2.8 ± 0.4 nm, respectively. Though the exciton diffusion length in PBDB-T-2F:IT-4Cl is not yet reported, the exciton diffusion lengths in other similar materials have been reported to be 5–20 nm. ^{39,68} The extracted ξ are in the same order of magnitude, indicating that the excitons can reach the D/A interfaces efficiently.

All of the FFT images in Figure S4b,d exhibit isotropic features, indicating the isotropic BHJs throughout the whole 1.2 μ m thick active layer. The aforementioned quantities and the FFT images of all measured dI/dV mappings are shown in Figures S5–S21 and summarized in Figure 4j–l. The domain perimeters, areas, and distance to the nearest D/A interface were extracted from 17 dI/dV images measured at nine distances to the Si/active layer interface. From the z-dependent histograms of domain size, APR, and ξ , as shown in Figure 4j–l, it can be concluded that the nanomorphology within the 1.2 μ m thick active layer is homogeneous. It indicates that the redistribution of the donor and acceptor molecules during the annealing process eliminated the influences from the solvent molecule evaporation process on the nanomorphology.

CONCLUSIONS

In summary, the molecular nanomorphologies of the PBDB-T-2F:IT-4Cl-based active layer are observed to be isotropic and uniform throughout a 1.2 μ m thick active layer. This XSTM/S method can be further used to study the nanomorphology of the active layer when near other interfaces, such as those with the PEDOT:PSS and/or ZnO. Further research is needed toward that direction. An intermediate domain between the donor-rich and acceptor-rich molecular domains is identified, with a thickness on the order of a few nm. The electronic energy gaps of donor-rich domains (PBDB-T-2F-rich), acceptor-rich domains (IT-4Cl-rich domains), and the intermediate or mixed domains are observed to be 2.54 \pm 0.09, 1.8 \pm 0.1,

and 2.3 ± 0.1 eV, respectively. By comparing with the reported absorption spectra of PBDB-T-2F and IT-4Cl, the exciton binding energies in PBDB-T-2F and IT-4Cl are estimated to be 0.74 and 0.32 eV, respectively. It is determined that there is an \sim 0.7 V loss in the open circuit voltage. These microscopic pictures of the PBDB-T-2F:IT-4Cl-based active layer may lead to new insights in OPV design and fundamental understandings.

ASSOCIATED CONTENT

Supporting Information

The Supporting Information is available free of charge at https://pubs.acs.org/doi/10.1021/acsami.1c18426.

SEM and STM images of the active layer in crosssectional geometry and Fourier transform analysis of these images (PDF)

AUTHOR INFORMATION

Corresponding Author

TeYu Chien — Department of Physics & Astronomy, University of Wyoming, Laramie, Wyoming 82071, United States; ⊙ orcid.org/0000-0001-7133-6650; Email: tchien@uwyo.edu

Authors

Rabindra Dulal – Department of Physics & Astronomy, University of Wyoming, Laramie, Wyoming 82071, United States

William R. Scougale – Department of Physics & Astronomy, University of Wyoming, Laramie, Wyoming 82071, United States

Wei Chen — Department of Mechanical Engineering, Northwestern University, Evanston, Illinois 60208, United States; orcid.org/0000-0002-4653-7124

Ganesh Balasubramanian — Department of Mechanical Engineering & Mechanics, Lehigh University, Bethlehem, Pennsylvania 18015, United States; orcid.org/0000-0003-1834-5501

Complete contact information is available at: https://pubs.acs.org/10.1021/acsami.1c18426

Author Contributions

The manuscript was written through contributions of all authors. All authors have given approval to the final version of the manuscript. R.D. performed all of the experiments. W.R.S. performed the domain analysis. R.D. and TY.C. analyzed the experimental results. R.D. and TY.C. wrote the manuscript. All authors edited and commented on the manuscript and helped with the analysis of the results. W.C., G.B., and TY.C. conceived the project.

Notes

The authors declare no competing financial interest.

ACKNOWLEDGMENTS

This work was supported by the National Science Foundation (NSF) under Award Nos. CMMI-1662435, 1662509, and 1753770.

REFERENCES

(1) Boudreault, P.-L. T.; Najari, A.; Leclerc, M. Processable Low-Bandgap Polymers for Photovoltaic Applications. *Chem. Mater.* **2011**, 23, 456–469.

- (2) Hou, J.; Chen, H. Y.; Zhang, S.; Li, G.; Yang, Y. Synthesis, Characterization, and Photovoltaic Properties of a Low Band Gap Polymer Based on Silole-Containing Polythiophenes and 2,1,3-Benzothiadiazole. *J. Am. Chem. Soc.* 2008, 130, 16144–16145.
- (3) Liang, Y.; Feng, D.; Wu, Y.; Tsai, S.-T.; Li, G.; Ray, C.; Yu, L. Highly Efficient Solar Cell Polymers Developed via Fine-Tuning of Structural and Electronic Properties. *J. Am. Chem. Soc.* **2009**, *131*, 7792–7799.
- (4) Bijleveld, J. C.; Gevaerts, V. S.; DiNuzzo, D.; Turbiez, M.; Mathijssen, S. C. J.; DeLeeuw, D. M.; Wienk, M. M.; Janssen, R. A. J. Efficient Solar Cells Based on an Easily Accessible Diketopyrrolopyrrole Polymer. *Adv. Mater.* **2010**, *22*, E242–E246.
- (5) Piliego, C.; Holcombe, T. W.; Douglas, J. D.; Woo, C. H.; Beaujuge, P. M.; Fréchet, J. M. J. Synthetic Control of Structural Order in N-Alkylthieno[3,4-c]Pyrrole-4,6-Dione-Based Polymers for Efficient Solar Cells. J. Am. Chem. Soc. 2010, 132, 7595–7597.
- (6) Yu, G.; Gao, J.; Hummelen, J. C.; Wudl, F.; Heeger, A. J. Polymer Photovoltaic Cells: Enhanced Efficiencies via a Network of Internal Donor-Acceptor Heterojunctions. *Science* **1995**, *270*, 1789–1791.
- (7) Li, G.; Chu, C. W.; Shrotriya, V.; Huang, J.; Yang, Y. Efficient Inverted Polymer Solar Cells. *Appl. Phys. Lett.* **2006**, 88, No. 253503.
- (8) Padinger, F.; Rittberger, R. S.; Sariciftci, N. S. Effects of Postproduction Treatment on Plastic Solar Cells. *Adv. Funct. Mater.* **2003**, *13*, 85–88.
- (9) Li, G.; Shrotriya, V.; Huang, J.; Yao, Y.; Moriarty, T.; Emery, K.; Yang, Y. High-Efficiency Solution Processable Polymer Photovoltaic Cells by Self-Organization of Polymer Blends. *Nat. Mater.* **2005**, *4*, 864–868.
- (10) Peet, J.; Kim, J. Y.; Coates, N. E.; Ma, W. L.; Moses, D.; Heeger, A. J.; Bazan, G. C. Efficiency Enhancement in Low-Bandgap Polymer Solar Cells by Processing with Alkane Dithiols. *Nat. Mater.* **2007**, *6*, 497–500.
- (11) Brabec, C. J.; Gowrisanker, S.; Halls, J. J. M.; Laird, D.; Jia, S.; Williams, S. P. Polymer-Fullerene Bulk-Heterojunction Solar Cells. *Adv. Mater.* **2010**, *22*, 3839–3856.
- (12) Chen, J.; Yong, C. Development of Novel Conjugated Donor Polymers for High-Efficiency Bulk-Heterojunction Photovoltaic Devices. *Acc. Chem. Res.* **2009**, *42*, 1709–1718.
- (13) Cheng, Y.; Jin, H.; Oh, J.; Huang, X.; Lv, R.; Huang, B.; Ma, Z.; Yang, C.; Chen, L.; Chen, Y. Structural Similarity Induced Improvement in the Performance of Organic Solar Cells Based on Novel Terpolymer Donors. J. Mater. Chem. A 2021, 9, 9238–9247.
- (14) Wienk, M. M.; Kroon, J. M.; Verhees, W. J. H.; Knol, J.; Hummelen, J. C.; VanHal, P. A.; Janssen, R. A. J. Efficient Methano[70]Fullerene/MDMO-PPV Bulk Heterojunction Photovoltaic Cells. *Angew. Chem., Int. Ed.* **2003**, *42*, 3371–3375.
- (15) Hummelen, J. C.; Knight, B. W.; Lepeq, F.; Wudl, F.; Yao, J.; Wilkins, C. L. Preparation and Characterization of Fulleroid and Methanofullerene Derivatives. J. Org. Chem. 1995, 60, 532–538.
- (16) Zhao, G. J.; He, Y. J.; Li, Y. 6.5% Efficiency of Polymer Solar Cells Based on Poly(3-Hexylthiophene) and Indene-C60 Bisadduct by Device Optimization. *Adv. Mater.* **2010**, *22*, 4355–4358.
- (17) Wang, C. L.; Zhang, W. B.; VanHorn, R. M.; Tu, Y.; Gong, X.; Cheng, S. Z. D.; Sun, Y.; Tong, M.; Seo, J.; Hsu, B. B. Y.; Heeger, A. J. A Porphyrin-Fullerene Dyad with a Supramolecular "Double-Cable" Structure as a Novel Electron Acceptor for Bulk Heterojunction Polymer Solar Cells. *Adv. Mater.* 2011, 23, 2951–2956.
- (18) Xu, H.; Liu, R.; Choudhary, A.; Chen, W. In A Machine Learning-Based Design Representation Method for Designing Heterogeneous Microstructures, ASME 2014 International Design Engineering Technical Conferences & Computers and Information in Engineering Conference; Buffalo, New York, 2014; pp IDETC2014-34570.
- (19) Chen, J. D.; Cui, C.; Li, Y. Q.; Zhou, L.; Ou, Q. D.; Li, C.; Li, Y.; Tang, J. X. Single-Junction Polymer Solar Cells Exceeding 10% Power Conversion Efficiency. *Adv. Mater.* **2015**, *27*, 1035–1041.
- (20) Kim, H. U.; Kim, J. H.; Suh, H.; Kwak, J.; Kim, D.; Grimsdale, A. C.; Yoon, S. C.; Hwang, D. H. High Open Circuit Voltage Organic Photovoltaic Cells Fabricated Using 9,9'-Bifluorenylidene as a Non-

- Fullerene Type Electron Acceptor. Chem. Commun. 2013, 49, 10950–10952.
- (21) Anctil, A.; Babbitt, C. W.; Raffaelle, R. P.; Landi, B. J. Material and Energy Intensity of Fullerene Production. *Environ. Sci. Technol.* **2011**, *45*, 2353–2359.
- (22) Scott, L. T. Methods for the Chemical Synthesis of Fullerenes. *Angew. Chem., Int. Ed.* **2004**, 43, 4994–5007.
- (23) Scharber, M. C.; Mühlbacher, D.; Koppe, M.; Denk, P.; Waldauf, C.; Heeger, A. J.; Brabec, C. J. Design Rules for Donors in Bulk-Heterojunction Solar Cells Towards 10% Energy-Conversion Efficiency. *Adv. Mater.* **2006**, *18*, 789–794.
- (24) Bundgaard, E.; Krebs, F. C. Low Band Gap Polymers for Organic Photovoltaics. *Sol. Energy Mater. Sol. Cells* **2007**, *91*, 954–985.
- (25) Zhang, M.; Zhu, L.; Zhou, G.; Hao, T.; Qiu, C.; Zhao, Z.; Hu, Q.; Larson, B. W.; Zhu, H.; Ma, Z.; Tang, Z.; Feng, W.; Zhang, Y.; Russell, T. P.; Liu, F. Single-Layered Organic Photovoltaics with Double Cascading Charge Transport Pathways: 18% Efficiencies. *Nat. Commun.* 2021, 12, No. 309.
- (26) Lin, Y.; Magomedov, A.; Firdaus, Y.; Kaltsas, D.; El-Labban, A.; Faber, H.; Naphade, D. R.; Yengel, E.; Zheng, X.; Yarali, E.; Chaturvedi, N.; Loganathan, K.; Gkeka, D.; AlShammari, S. H.; Bakr, O. M.; Laquai, F.; Tsetseris, L.; Getautis, V.; Anthopoulos, T. D. 18.4% Organic Solar Cells Using a High Ionization Energy Self-Assembled Monolayer as Hole-Extraction Interlayer. *ChemSusChem* 2021, 14, 3569–3578.
- (27) Liu, Q.; Jiang, Y.; Jin, K.; Qin, J.; Xu, J.; Li, W.; Xiong, J.; Liu, J.; Xiao, Z.; Sun, K.; Yang, S.; Zhang, X.; Ding, L. 18% Efficiency Organic Solar Cells. *Sci. Bull.* **2020**, *65*, 272–275.
- (28) Rand, B. P.; Burk, D. P.; Forrest, S. R. Offset Energies at Organic Semiconductor Heterojunctions and Their Influence on the Open-Circuit Voltage of Thin-Film Solar Cells. *Phys. Rev. B* **2007**, *75*, No. 115327.
- (29) Koster, L. J. A.; Mihailetchi, V. D.; Ramaker, R.; Blom, P. W. M. Light Intensity Dependence of Open-Circuit Voltage of Polymer:-Fullerene Solar Cells. *Appl. Phys. Lett.* **2005**, *86*, No. 123509.
- (30) Riede, M.; Mueller, T.; Tress, W.; Schueppel, R.; Leo, K. Small-Molecule Solar Cells Status and Perspectives. *Nanotechnology* **2008**, *19*, No. 424001.
- (31) Gruber, M.; Wagner, J.; Klein, K.; Hörmann, U.; Opitz, A.; Stutzmann, M.; Brütting, W. Thermodynamic Efficiency Limit of Molecular Donor-Acceptor Solar Cells and Its Application to Diindenoperylene/C 60 -Based Planar Heterojunction Devices. *Adv. Energy Mater.* **2012**, *2*, 1100–1108.
- (32) Veldman, D.; Meskers, S. C. J.; Janssen, R. A. J. The Energy of Charge-Transfer States in Electron Donor-Acceptor Blends: Insight into the Energy Losses in Organic Solar Cells. *Adv. Funct. Mater.* **2009**, *19*, 1939–1948.
- (33) Vandewal, K.; Tvingstedt, K.; Gadisa, A.; Inganäs, O.; Manca, J. V. Relating the Open-Circuit Voltage to Interface Molecular Properties of Donor:Acceptor Bulk Heterojunction Solar Cells. *Phys. Rev. B* **2010**, *81*, No. 125204.
- (34) Dennler, G.; Scharber, M. C.; Brabec, C. J. Polymer-Fullerene Bulk-Heterojunction Solar Cells. *Adv. Mater.* **2009**, *21*, 1323–1338.
- (35) Shih, M.-C.; Huang, B.-C.; Lin, C.-C.; Li, S.-S.; Chen, H.-A.; Chiu, Y.-P.; Chen, C.-W. Atomic-Scale Interfacial Band Mapping across Vertically Phased-Separated Polymer/Fullerene Hybrid Solar Cells. *Nano Lett.* **2013**, *13*, 2387–2392.
- (36) Zhang, H.; Yao, H.; Hou, J.; Zhu, J.; Zhang, J.; Li, W.; Yu, R.; Gao, B.; Zhang, S.; Hou, J. Over 14% Efficiency in Organic Solar Cells Enabled by Chlorinated Nonfullerene Small-Molecule Acceptors. *Adv. Mater.* **2018**, *30*, No. 1800613.
- (37) Zhang, Y.; Yao, H.; Zhang, S.; Qin, Y.; Zhang, J.; Yang, L.; Li, W.; Wei, Z.; Gao, F.; Hou, J. Fluorination vs. Chlorination: A Case Study on High Performance Organic Photovoltaic Materials. *Sci. China Chem.* **2018**, *61*, 1328–1337.
- (38) Munshi, J.; Dulal, R.; Chien, T.; Chen, W.; Balasubramanian, G. Solution Processing Dependent Bulk Heterojunction Nano-

- morphology of P3HT/PCBM Thin Films. ACS Appl. Mater. Interfaces 2019, 11, 17056-17067.
- (39) Berger, P. R.; Kim, M. Polymer Solar Cells: P3HT:PCBM and Beyond. J. Renewable Sustainable Energy 2018, 10, No. 013508.
- (40) Ghumman, U. F.; Iyer, A.; Dulal, R.; Munshi, J.; Wang, A.; Chien, T.; Balasubramanian, G.; Chen, W. A Spectral Density Function Approach for Active Layer Design of Organic Photovoltaic Cells. J. Mech. Des. 2018, 140, No. 111408.
- (41) Salvatori, P.; Mosconi, E.; Wang, E.; Andersson, M.; Muccini, M.; DeAngelis, F. Computational Modeling of Isoindigo-Based Polymers Used in Organic Solar Cells. *J. Phys. Chem. C* **2013**, *117*, 17940–17954.
- (42) Iyer, A.; Dulal, R.; Zhang, Y.; Ghumman, U. F.; Chien, T. Y.; Balasubramanian, G.; Chen, W. Designing Anisotropic Microstructures with Spectral Density Function. *Comput. Mater. Sci.* **2020**, 179, No. 109559.
- (43) Ghumman, U. F.; Iyer, A.; Dulal, R.; Munshi, J.; Wang, A.; Chien, T.; Balasubramanian, G.; Chen, W. In *A Spectral Density Function Approach for Design of Organic Photovoltaic Cells*, International Design Engineering Technical Conferences and Computers and Information in Engineering Conference; American Society of Mechanical Engineers, 2018; p V02BT03A015.
- (44) Munshi, J.; Ghumman, U. F.; Iyer, A.; Dulal, R.; Chen, W.; Chien, T.; Balasubramanian, G. Effect of Polydispersity on the Bulk-Heterojunction Morphology of P3HT:PCBM Solar Cells. *J. Polym. Sci., Part B: Polym. Phys.* **2019**, *57*, 895–903.
- (45) Bagui, A.; Iyer, S. S. K. Effect of Solvent Annealing in the Presence of Electric Field on P3HT:PCBM Films Used in Organic Solar Cells. *IEEE Trans. Electron Devices* **2011**, *58*, 4061–4066.
- (46) Masters, R. C.; Wan, Q.; Zhang, Y.; Dapor, M.; Sandu, A. M.; Jiao, C.; Zhou, Y.; Zhang, H.; Lidzey, D. G.; Rodenburg, C. Novel Organic Photovoltaic Polymer Blends: A Rapid, 3-Dimensional Morphology Analysis Using Backscattered Electron Imaging in the Scanning Electron Microscope. Sol. Energy Mater. Sol. Cells 2017, 160, 182–192.
- (47) Kiel, J. W.; Kirby, B. J.; Majkrzak, C. F.; Maranville, B. B.; Mackay, M. E. Nanoparticle Concentration Profile in Polymer-Based Solar Cells. *Soft Matter* **2010**, *6*, 641–646.
- (48) Dulal, R.; Iyer, A.; Ghumman, U. F.; Munshi, J.; Wang, A.; Balasubramanian, G.; Chen, W.; Chien, T. Elongated Nanodomains and Molecular Intermixing Induced Doping in Organic Photovoltaic Active Layers with Electric Field Treatment. *ACS Appl. Polym. Mater.* **2020**, *2*, 335–341.
- (49) Apaydın, D. H.; Yildiz, D. E.; Cirpan, A.; Toppare, L. Optimizing the Organic Solar Cell Efficiency: Role of the Active Layer Thickness. Sol. Energy Mater. Sol. Cells 2013, 113, 100–105.
- (50) Namkoong, G.; Kong, J.; Samson, M.; Hwang, I. W.; Lee, K. Active Layer Thickness Effect on the Recombination Process of PCDTBT:PC71BM Organic Solar Cells. *Org. Electron.* **2013**, *14*, 74–79.
- (51) Zhang, Y.; Feng, H.; Meng, L.; Wang, Y.; Chang, M.; Li, S.; Guo, Z.; Li, C.; Zheng, N.; Xie, Z.; Wan, X.; Chen, Y. High Performance Thick-Film Nonfullerene Organic Solar Cells with Efficiency over 10% and Active Layer Thickness of 600 Nm. Adv. Energy Mater. 2019, 9, No. 1902688.
- (52) Katayama, M.; Kaji, T.; Nakao, S.; Hiramoto, M. Ultra-Thick Organic Pigment Layer Up to 10 Mm Activated by Crystallization in Organic Photovoltaic Cells. *Front. Energy Res.* **2020**, *8*, No. 4.
- (53) Ulum, M. S.; Sesa, E.; Kasman; Belcher, W. The Effect of Active Layer Thickness on P3HT:PCBM Nanoparticulate Organic Photovoltaic Device Performance. *J. Phys.: Conf. Ser.* **2019**, *1242*, No. 012025.
- (54) Murphy, L.; Hong, W.; Aziz, H.; Li, Y. Organic Photovoltaics with Thick Active Layers (~800 Nm) Using a High Mobility Polymer Donor. Sol. Energy Mater. Sol. Cells 2013, 114, 71–81.
- (55) Li, G.; Shrotriya, V.; Yao, Y.; Yang, Y. Investigation of Annealing Effects and Film Thickness Dependence of Polymer Solar Cells Based on Poly(3-Hexylthiophene). *J. Appl. Phys.* **2005**, *98*, No. 043704.

- (56) Min Nam, Y.; Huh, J.; Ho Jo, W. Optimization of Thickness and Morphology of Active Layer for High Performance of Bulk-Heterojunction Organic Solar Cells. *Sol. Energy Mater. Sol. Cells* **2010**, 94, 1118–1124.
- (57) Moulé, A. J.; Bonekamp, J. B.; Meerholz, K. The Effect of Active Layer Thickness and Composition on the Performance of Bulk-Heterojunction Solar Cells. *J. Appl. Phys.* **2006**, *100*, No. 094503.
- (58) Yost, A. J.; Pimachev, A.; Ho, C. C.; Darling, S. B.; Wang, L.; Su, W. F.; Dahnovsky, Y.; Chien, T. Coexistence of Two Electronic Nano-Phases on a CH3NH3PbI3-XClxSurface Observed in STM Measurements. ACS Appl. Mater. Interfaces 2016, 8, 29110–29116.
- (59) Wang, A.; Chien, T. Perspectives of Cross-Sectional Scanning Tunneling Microscopy and Spectroscopy for Complex Oxide Physics. *Phys. Lett. A* **2018**, 382, 739–748.
- (60) Shih, M. C.; Huang, B. C.; Lin, C. C.; Li, S. S.; Chen, H. A.; Chiu, Y. P.; Chen, C. W. Atomic-Scale Interfacial Band Mapping across Vertically Phased-Separated Polymer/Fullerene Hybrid Solar Cells. *Nano Lett.* **2013**, *13*, 2387–2392.
- (61) Horcas, I.; Fernández, R.; Gómez-Rodríguez, J. M.; Colchero, J.; Gómez-Herrero, J.; Baro, A. M. WSXM: A Software for Scanning Probe Microscopy and a Tool for Nanotechnology. *Rev. Sci. Instrum.* **2007**, *78*, No. 013705.
- (62) Chen, X.; Liu, H.; Xia, L.; Hayat, T.; Alsaedi, A.; Tan, Z. A Pentacyclic: S, N -Heteroacene Based Electron Acceptor with Strong near-Infrared Absorption for Efficient Organic Solar Cells. *Chem. Commun.* **2019**, *55*, 7057–7060.
- (63) Deibel, C.; MacK, D.; Gorenflot, J.; Schöll, A.; Krause, S.; Reinert, F.; Rauh, D.; Dyakonov, V. Energetics of Excited States in the Conjugated Polymer Poly(3- Hexylthiophene). *Phys. Rev. B* **2010**, *81*, No. 085202.
- (64) Qiu, Z.; Trushin, M.; Fang, H.; Verzhbitskiy, I.; Gao, S.; Laksono, E.; Yang, M.; Lyu, P.; Li, J.; Su, J.; Telychko, M.; Watanabe, K.; Taniguchi, T.; Wu, J.; Neto, A. H. C.; Yang, L.; Eda, G.; Adam, S.; Lu, J. Giant Gate-Tunable Bandgap Renormalization and Excitonic Effects in a 2D Semiconductor. *Sci. Adv.* **2019**, *5*, No. eaaw2347.
- (65) Zhu, L.; Tu, Z.; Yi, Y.; Wei, Z. Achieving Small Exciton Binding Energies in Small Molecule Acceptors for Organic Solar Cells: Effect of Molecular Packing. *J. Phys. Chem. Lett.* **2019**, *10*, 4888–4894.
- (66) Bhatta, R. S.; Tsige, M. Chain Length and Torsional Dependence of Exciton Binding Energies in P3HT and PTB7 Conjugated Polymers: A First-Principles Study. *Polymer* **2014**, *55*, 2667–2672.
- (67) Bradski, G. The OpenCV Library. Dr. Dobb's J. Softw. Tools 2000, 25, 120-125.
- (68) Zhang, J.; Kan, B.; Pearson, A. J.; Parnell, A. J.; Cooper, J. F. K.; Liu, X. K.; Conaghan, P. J.; Hopper, T. R.; Wu, Y.; Wan, X.; Gao, F.; Greenham, N. C.; Bakulin, A. A.; Chen, Y.; Friend, R. H. Efficient Non-Fullerene Organic Solar Cells Employing Sequentially Deposited Donor-Acceptor Layers. J. Mater. Chem. A 2018, 6, 18225–18233.